JYX
JYVÄSKYLÄN YLIOPISTO
UNIVERSITY OF JYVÄSKYLÄ

This is a self-archived version of an original article. This version may differ from the original in pagination and typographic details.

Author(s): Barthel, Armin; Roberts, Joseph; Napari, Mari; Frentrup, Martin; Huq, Tahmid; Kovács, András; Oliver, Rachel; Chalker, Paul; Sajavaara, Timo; Massabuau, Fabien

Title: Ti Alloyed α-Ga2O3 : route towards Wide Band Gap Engineering

Year: 2020

Version: Published version

Copyright: © 2020 the Authors

Rights: CC BY 4.0

Rights url: https://creativecommons.org/licenses/by/4.0/

Please cite the original version:

Barthel, A., Roberts, J., Napari, M., Frentrup, M., Huq, T., Kovács, A., Oliver, R., Chalker, P., Sajavaara, T., & Massabuau, F. (2020). Ti Alloyed α-Ga2O3 : route towards Wide Band Gap Engineering. Micromachines, 11(12), Article 1128. https://doi.org/10.3390/mi11121128

micromachines

MDPI

Article

Ti Alloyed α-Ga_2O_3: Route towards Wide Band Gap Engineering

Armin Barthel [1,*], Joseph Roberts [2], Mari Napari [1,3], Martin Frentrup [1], Tahmida Huq [1], András Kovács [4], Rachel Oliver [1], Paul Chalker [2] and Timo Sajavaara [5] and Fabien Massabuau [1,6,*]

1 Department of Materials Science and Metallurgy, University of Cambridge, Cambridge CB3 0FS, UK; m.p.napari@soton.ac.uk (M.N.); mf562@cam.ac.uk (M.F.); tnh25@cam.ac.uk (T.H.); rao28@cam.ac.uk (R.O.)
2 School of Engineering, The University of Liverpool, Liverpool L69 3GH, UK; j.w.roberts@liverpool.ac.uk (J.R.); pchalker@liverpool.ac.uk (P.C.)
3 Zepler Institute for Photonics and Nanoelectronics, University of Southampton, Southampton SO17 1BJ, UK
4 Ernst Ruska-Centre for Microscopy and Spectroscopy with Electrons and Peter Grünberg Institute, Forschungszentrum Jülich, 52425 Jülich, Germany; a.kovacs@fz-juelich.de
5 Department of Physics, University of Jyväskylä, FI-40014 Jyväskylä, Finland; timo.sajavaara@jyu.fi
6 Department of Physics, SUPA, University of Strathclyde, Glasgow G4 0NG, UK
* Correspondence: ab2301@cam.ac.uk (A.B.); f.massabuau@strath.ac.uk (F.M.)

Received: 3 November 2020; Accepted: 15 December 2020; Published: 20 December 2020

Abstract: The suitability of Ti as a band gap modifier for α-Ga_2O_3 was investigated, taking advantage of the isostructural α phases and high band gap difference between Ti_2O_3 and Ga_2O_3. Films of $(Ti,Ga)_2O_3$ were synthesized by atomic layer deposition on sapphire substrates, and characterized to determine how crystallinity and band gap vary with composition for this alloy. We report the deposition of high quality α-$(Ti_xGa_{1-x})_2O_3$ films with x = 3.7%. For greater compositions the crystalline quality of the films degrades rapidly, where the corundum phase is maintained in films up to x = 5.3%, and films containing greater Ti fractions being amorphous. Over the range of achieved corundum phase films, that is $0\% \leq x \leq 5.3\%$, the band gap energy varies by ~ 270 meV. The ability to maintain a crystalline phase at low fractions of Ti, accompanied by a modification in band gap, shows promising prospects for band gap engineering and the development of wavelength specific solar-blind photodetectors based on α-Ga_2O_3.

Keywords: gallium oxide; wide band gap semiconductors; solar-blind detection; atomic layer deposition; thin films; alloying; bandgap

1. Introduction

Alpha phase gallium oxide (α-Ga_2O_3) is an ultra-wide band gap semiconductor, with most measurements of its band gap lying between 5.1 eV and 5.3 eV [1–5]. It is of particular interest for applications in solar-blind ultraviolet (UV) photodetectors [2,4,6,7]. Uses for photodetectors that can absorb efficiently in this regime, of wavelengths < 285 nm, include water and air purification systems [8], flame detection, UV astronomy, missile defence systems and engine monitoring [4,9].

α-Ga_2O_3 is a metastable phase of Ga_2O_3, a polymorphic group-III sesquioxide, with commonly reported phases α, β, γ, and ε [10] as well as the more recent κ [11]. Previous research on this material has been mostly focused on the stable, monoclinic β phase [10,12,13], however, due to recent advances in thin film growth techniques, such as mist chemical vapour deposition (mist-CVD) [1,14,15] and atomic layer deposition (ALD) [4,5,16,17], it has become possible to synthesise high quality films of α-Ga_2O_3. These films are grown epitaxially on sapphire (α-Al_2O_3), which shares its rhombohedral

corundum crystal structure [1] (inset Figure 1) with α-Ga_2O_3. This has been achieved at temperatures as low as 250 °C by ALD [4,5,16] and the material has been successfully integrated into solar-blind UV photodetectors, already showing an advantage over photodetectors based on β-Ga_2O_3, by having shorter response times [4].

Apart from sapphire, the corundum crystal structure is also shared by many other semiconducting sesquioxides [18–20], as shown in Figure 1, providing great potential for band gap engineering [15,21]. Band gap engineering in the solar-blind region would be pivotal for producing layered device structures and for tuning the application of devices, for example, by producing wavelength-specific biochemical or flame sensors where the material would be tuned to match the peak absorption wavelength of a given micro-organism or molecule [22,23]. Previously, alloying of corundum phase Ga_2O_3 with Al_2O_3 [24], In_2O_3 [25], Cr_2O_3 [19], Fe_2O_3 [19,20] and Rh_2O_3 [26] has been attempted.

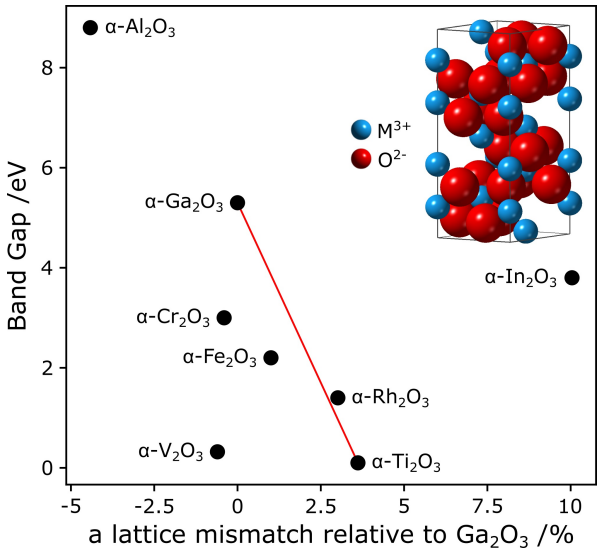

Figure 1. Diagram of the corundum phase semiconducting sesquioxide design space, centered on α-Ga_2O_3. The band gaps of the materials [1,27–35] are plotted against their 'a' lattice parameters relative to α-Ga_2O_3 [36–42]. The red line indicates the alloys of α-Ti_2O_3 and α-Ga_2O_3, assuming that the band gap varies linearly with the lattice constants. Inset: Rhombohedral, corundum crystal structure of M_2O_3 (M: metal).

The aim of this work is to study the feasibility of using Ti as a band gap modifier for α-Ga_2O_3, by characterizing a number of oxide films grown by ALD with different Ti to Ga ratios. α-Ti_2O_3 adopts the corundum crystal structure [39,43] with lattice parameters: a = 5.157 Å and c = 13.613 Å [39], giving a relatively small lattice mismatch of about 3.5% with α-Ga_2O_3 (a = 4.983 Å and c = 13.433 Å [36]). Its direct band gap of 0.1 eV [29,30] is very small relative to that of α-Ga_2O_3, such that a band gap engineering over a few 100 meV (required for wavelength specific solar-blind photodetectors) would be achievable by alloying α-Ga_2O_3 with only very small amounts of α-Ti_2O_3. An even wider range of band gaps may be achievable, provided that an alloy of the two sesquioxides exhibits miscibility and crystallinity across a range of Ti:Ga ratios. This may be inhibited if Ti adopts a +4 oxidation state and preferentially forms TiO_2, which would not have a corundum structure. In β-Ga_2O_3, Ti was found to incorporate in the Ga_2O_3 host material for low compositions, but led to a phase separated Ga_2O_3-TiO_2 composite at greater compositions [44–46]. In the present study it is hoped that the shared corundum structure and low lattice mismatch between α-Ga_2O_3 and α-Ti_2O_3 would allow to alleviate these issues. Another property of α-Ti_2O_3 that is of interest is that it is a p-type semiconductor [30]. Alloying with Ti_2O_3 could thus provide a route to achieve p-type conductivity in α-Ga_2O_3, as was also demonstrated in an α phase Rh:Ga_2O_3 alloy by Kaneko et al. [26].

2. Experimental Methods

Ga_2O_3 and $(Ti,Ga)_2O_3$ thin films were grown using an Oxford Instruments OpAL plasma enhanced atomic layer deposition (PEALD) reactor. All films were grown on 0.25° miscut c-plane sapphire substrates with a temperature of 250 °C and chamber wall temperatures set to 150 °C. Triethylgallium (TEGa) from Epichem and Titanium(IV) Isopropoxide (TTIP) from Sigma-Aldrich were used as Ga and Ti precursors, respectively. The TEGa and TTIP precursors were held at 30 °C and 80 °C, respectively, with line temperatures for both precursors set at 90 °C and 100 °C, increasing in temperature closer to the reaction chamber. One cycle of Ga_2O_3 consisted of 0.1 s TEGa with 100 sccm Ar bubbling, 5 s 100 sccm Ar purge, 3 s O_2 flow stabilisation, 5 s 20 sccm 300 W O_2 plasma, 5 s 100 sccm Ar purge. One cycle of TiO_x consisted of 2 s TTIP with 100 sccm Ar bubbling, 10 s 100 sccm Ar purge, 0.04 s H_2O, 10 s 100 sccm Ar purge. The chosen growth parameters were adapted from Ref. [47]. Supercycles of Ga_2O_3 and TiO_x were used to produce Ti alloyed Ga_2O_3 films, with cycle ratios (TiO_x:Ga_2O_3) of 0:1, 1:32, 1:19, 1:9, 1:4 and 1:1, which are hereafter referred to as samples 0%Ti, 3%Ti, 5%Ti, 10%Ti, 20%Ti and 50%Ti, respectively. 500 total cycles were used for the 0%Ti film, 429 cycles for the 3 %Ti film and 400 cycles for the remaining films. Film thicknesses after growth were measured using a HORIBA Jobin Yvon spectroscopic ellipsometer fitted to a mixed Cauchy β-Ga_2O_3/TiO_2 model and are shown in Table 1. We estimate the film thicknesses obtained using this approach to be within ~10 % accuracy, due to the model itself.

The Ti:Ga ratio of the samples was determined using Rutherford backscattering spectrometry (RBS) with 1.615 MeV He^+ incident beam from a 1.7 MV Pelletron accelerator. The samples were tilted to 5° and the scattering angle was 165°. The measured spectra were analysed in the SimNRA program [48] which was used to calculate the Ti:Ga ratios from the respective peak areas in the raw data and weighting them against the corresponding Rutherford scattering cross-sections. Given that the peaks are clearly separated, no fitting was required to analyse these data.

The crystallinity of the samples was assessed by X-ray diffraction (XRD). A PANalytical Empyrean diffractometer was used with a Cu source and a hybrid two-bounce primary monochromator giving Cu Kα_1 radiation, and either a two-bounce Ge crystal analyser, for 2θ-ω scans, or a PIXcel detector, for reciprocal space maps (RSMs).

High-angle annular dark field scanning transmission electron microscopy (HAADF-STEM) using an aberration-corrected FEI Titan [49] operated at 200 kV was used to observe the sub-surface structure of the samples observed in cross-section. The annular dark field detector semi-angle used was 69.1 mrad. Compositional mapping was obtained using energy dispersive X-ray spectroscopy (EDX) in the same microscope and strain mapping was obtained using geometrical phase analysis [50]. The samples were prepared for imaging using standard mechanical grinding followed by Ar^+ ion milling at 5 kV and cleaning at 0.1–1 kV.

The surface morphology of the samples was investigated by atomic force microscopy (AFM) in a Bruker Dimension Icon operated in peak force tapping mode. Bruker SCANASYST-AIR tips with a nominal radius of 2 nm were used.

The band gaps of the films were determined from transmittance spectra of the films, measured using a Cary 7000 UV-VIS-NIR spectrometer in the range 200–800 nm. The system was calibrated for 100% and 0% transmittance.

Table 1. Summary of film characteristics. Samples are named after the percentage of Ti ALD cycles used for growth. Film thicknesses, obtained by ellipsometry, are estimates, since an appropriate fitting model for α-Ga_2O_3, amorphous Ga_2O_3 or α-Ti_2O_3 was unavailable. Composition, measured by RBS, represents the amount of Ti relative to Ga in the films. RMS roughness and band gaps were determined by AFM and UV-vis transmittance spectroscopy, respectively.

Sample	Thickness/nm	Composition x/%	RMS Roughness/nm	Band Gap/eV
0%Ti	33 ± 3	0	0.71 ± 0.01	~ 5.04
3%Ti	22 ± 2	3.7 ± 0.4	0.49 ± 0.02	~ 4.88
5%Ti	21 ± 2	5.3 ± 0.4	0.30 ± 0.01	~ 4.77
10%Ti	21 ± 2	12.8 ± 0.8	0.22 ± 0.01	~ 4.78
20%Ti	21 ± 2	23.1 ± 1.0	0.19 ± 0.01	~ 4.63
50%Ti	16 ± 2	61 ± 3	0.16 ± 0.01	~ 3.91

3. Results and Discussion

RBS was used for compositional analysis of the films. The main quantity of interest was the ratio of Ti to Ga in the films. RBS spectra were obtained for each film, showing peaks for Ga and Ti (except in the pure Ga_2O_3 sample) clearly separated due to the difference in atomic mass, as well as steps associated with Al and O from the sapphire substrate. The compositions x, here defined as x = at.%Ti /(at.%Ti + at.%Ga), attained from the integrated counts of the Ti and Ga peaks in the RBS spectra and corrected for by the respective Rutherford scattering cross sections, are tabulated in Table 1. The film compositions determined by RBS, are in relatively good agreement with those predicted from the ALD cycle ratios, deviating by about 10–30%. Deviations resulting from unequal growth rates of the different species are expected in ALD, with the growth being strongly affected by several factors, including temperature, chemistry of the precursors used, and the growth surface [51,52].

XRD was used to study the crystallinity of the films. The measured 2θ-ω XRD scans (Figure 2a) show the 0 0 0 6 reflection from the sapphire substrate and, for the 3 samples of lowest Ti fraction, also a peak from the film.

The pure α-Ga_2O_3 sample (sample 0%Ti) gives the peak of greatest intensity at $2\theta = 40.16°$, which is within the range of reported values in epitaxial films (40.05°–40.25° [1,16,36]). Differences in lattice parameter may be due to residual strain from the epitaxial relationship with the substrate. (Annealing the samples at approximately 400 °C has been shown to release that residual strain [7]). Interference fringes can be distinguished on the base of the diffraction peak, with a spacing that is representative of the film thickness—here 28 nm, in reasonable agreement with the thickness estimated by ellipsometry (Table 1).

As the concentration of Ti increases, the $(Ti,Ga)_2O_3$ peak becomes broader and weaker, vanishing completely for samples 20%Ti and 50%Ti, which is typical for amorphous materials with very short range order only. For those diffractograms where peaks are observed, that is, for compositions up to 5.3%, the $(Ti,Ga)_2O_3$ peak shifts to smaller angles as the Ti content increases, indicating that the lattice parameter of the crystal increases. This is expected, as the lattice parameters of α-Ti_2O_3 are larger and suggests that Ti has been incorporated into the films to form an α-$(Ti_xGa_{1-x})_2O_3$ alloy. However, the measured c lattice parameters exceed those expected from the compositions calculated from RBS data, using literature values for lattice parameters and assuming the applicability of Vegard's Law [53,54]. A likely cause of this is that the α-$(Ti_xGa_{1-x})_2O_3$ layers are compressively strained onto the sapphire substrate. However, due to insufficiently strong signals, it was not possible to verify and quantify the strain in the films by conducting a strain analysis from RSMs of symmetric and asymmetric reflections.

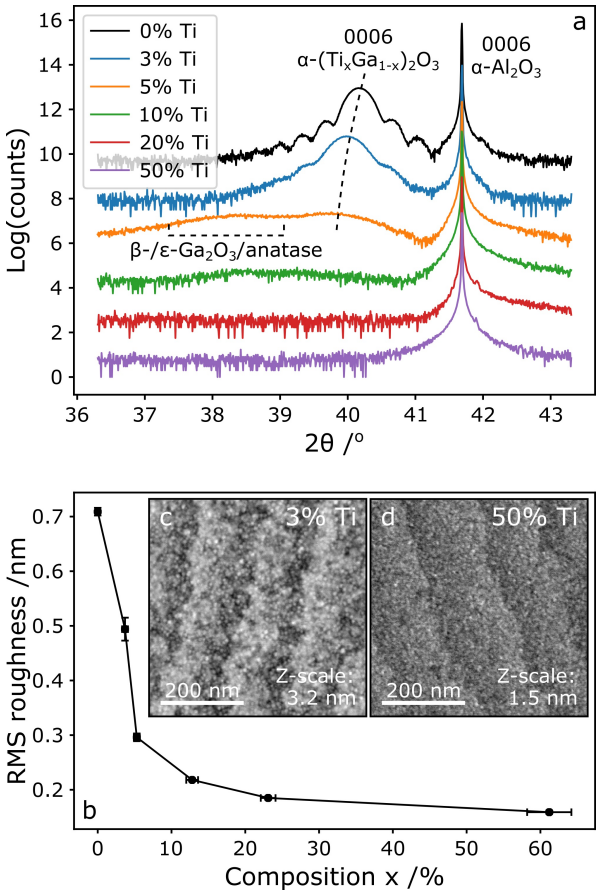

Figure 2. (**a**) 2θ-ω XRD scans of the symmetric 0 0 0 6 reflection of the α phase. (**b**) Variation of RMS surface roughness with Ti concentration. (**c**,**d**) 500 nm size AFM images of the 3%Ti (**c**) and 50%Ti (**d**) samples.

Lastly, for sample 5%Ti we note the presence of a second, broad and weak, peak located at a lower angle ($\sim$38°) than the α-$(Ti_xGa_{1-x})_2O_3$ peak (indicated in Figure 2a). Although it is too broad and weak to be uniquely identified, this peak could indicate the presence of one or more additional phases such as β-Ga_2O_3, ε-Ga_2O_3 or anatase TiO_2 in this film.

The surface topography of each sample was obtained by AFM and the root mean square (RMS) roughness determined at a 500 nm scan size. The AFM images (Figure 2c,d) are representative of the topographies observed for all samples. The surface was smooth on a nanometer scale, as shown by the RMS roughness given in Table 1 and Figure 2b.

The surface of all samples also bears ledges with a constant spacing, mostly independent of Ti content. These ledges likely arise from the morphology of the sapphire substrates, which, due to having a miscut angle of 0.25°, also have steps on the surface. These provide two distinct regions: a flat (0 0 0 1) oriented surface and the step. Given preferential growth at one of these sites in ALD, a step pattern with the same spacing would be expected. A topographical scan of a pristine sapphire wafer (not shown here) shows similar step widths as Figure 2c,d.

The surfaces of the low Ti fraction samples (Figure 2c) exhibit small grains of the order of 1–10 nm, presumably due to the termination of α phase columns as was observed in Refs. [5,16]. As the Ti fraction increases (Figure 2d) these features cannot be identified anymore, which may indicate that the films are amorphous, in line with our XRD results. The plot of the RMS roughness vs. Ti fraction (Figure 2b) shows that the roughness decreases quickly with Ti fraction. This decrease in RMS roughness coincides with the disappearance of the small grain features as the Ti fraction increases. This trend (together with the images Figure 2c,d as well as XRD results Figure 2a) implies that the low Ti fraction ($x \leq 5.3\%$) films are crystalline, whilst the films with high Ti fraction ($x \geq 12.8\%$) are amorphous.

STEM was used to analyse a cross section of sample 3%Ti, allowing the interface between substrate and film to be studied as well as giving a local insight to crystallinity, strain and composition across the film. The results are compiled in Figure 3, showing large, vaguely columnar regions of crystallinity in the film (two such columns are outlined in Figure 3a) with, in places, regions of amorphous material. This is in agreement with prior work on ALD grown, pure α-Ga_2O_3 [16]. The film thickness measured by HAADF-STEM images (Figure 3a) is consistent with that measured by ellipsometry. We also note that the film is continuous with a fairly uniform thickness, exhibiting only sub-nanometre variation in surface height that is consistent with the low surface roughness obtain from AFM (Figure 2c). The high resolution data and Fast-Fourier transforms (FFT) of the film and substrate regions (Figure 3b) confirm that the film has the corundum structure with the epitaxial relationship with the sapphire substrate being $\langle 11\bar{2}0\rangle_{Al_2O_3} \parallel \langle 11\bar{2}0\rangle_{(Ti_xGa_{1-x})_2O_3}$ and $[0002]_{Al_2O_3} \parallel [0002]_{(Ti_xGa_{1-x})_2O_3}$, in agreement with previous studies [16].

Observation of the interface region reveals the presence of a high density of periodically spaced misfit dislocations, with an average spacing of 4.9 ± 0.4 nm. Apart from these, there are also some dislocations located within the film, approximately 1–3 nm from the interface (not shown here) although these are more rare. The misfit dislocations at the interface can be easily seen in Figure 3b,c (indicated by arrows), the latter showing them as dipoles of tensile and compressive strain. Figure 3e shows two misfit dislocations at greater magnification such that it is possible to count the number of lattice planes between them. They are separated by $23 \times d_{11\bar{2}0\,Al_2O_3}$ or $22 \times d_{11\bar{2}0\,(Ti_xGa_{1-x})_2O_3}$. This indicates that the film is almost fully relaxed (nominally $22 \times d_{11\bar{2}0\,Al_2O_3} = 5.232$ nm, $21 \times d_{11\bar{2}0\,Ga_2O_3} = 5.232$ nm and $21 \times d_{11\bar{2}0\,(Ti_xGa_{1-x})_2O_3} = 5.238$ nm assuming x = 3.7%). The strain maps in Figure 3c,d confirm that all the strain relaxation occurs at the interface, and that the strain is otherwise uniform throughout the film. The strain relaxation of the film observed in STEM is in contradiction with the XRD data, which instead suggests that the film is strained. A possible explanation may be that these probe the material at different scales: TEM focuses on a small nanometre-scale region of the sample—typically looking at the scale of an individual column—whereas XRD looks at average/global properties of the film. Another possibility is that the observed imperfect spacing of the misfit dislocations for $(Ti_xGa_{1-x})_2O_3$ is unable to fully accommodate the strain.

EDS analysis of the film shows that the distribution of Ti across the film was uniform, with no visible segregation (Figure 3a). Compositional analysis using Cliff-Lorimer method yielded a composition of $x \sim 5\%$, which is in fair agreement with the RBS data (we note however that EDS quantification is here less reliable than the RBS data, because the sample was imaged on the zone-axis for the α phase and was therefore susceptible to interference from electron channeling).

UV-vis transmittance spectroscopy was conducted to attain the optical band gap of the films. Only transmittance spectra were taken. Ignoring reflected intensity is justified by the fact that the films were transparent and only weakly reflecting to the eye, at normal incidence. Using the assumption of negligible reflectance, Beer-Lambert law could be applied to calculate absorptivity from the transmittance [2,55]. Film transmittances were isolated from the transmittances of the samples by measuring that of a reference pristine sapphire substrate. Absorptivity could then be used to produce Tauc plots using the relation in Equation (1), from which the band gap was determined. A Tauc exponent of $n = \frac{1}{2}$ for a direct energy band gap and allowed transition was used, as was also applied in other works [1–5]:

$$\alpha h\nu \propto (h\nu - E_g)^n. \quad (1)$$

The collected transmittance spectra for the films are depicted in Figure 4 with an inset of the Tauc plots used to attain the band gap energy. The transmittance spectra clearly show that the absorption edge shifts to longer wavelengths as the Ti concentration of the films increases—as is represented by the band gap energies values listed in Table 1. Above the absorption edge, the transmittance is very high, suggesting that the assumption of little reflection or scattering, when calculating absorptivity is justified (the small discontinuity in the spectrum at ~ 350 nm is a systematic instrumental error, due to

the source change that occurs in the system at that wavelength). The transmittance at wavelengths longer than the absorption edge seems to decrease with increasing Ti concentration, which could be due to increased scattering or reflection from the films which are not crystalline.

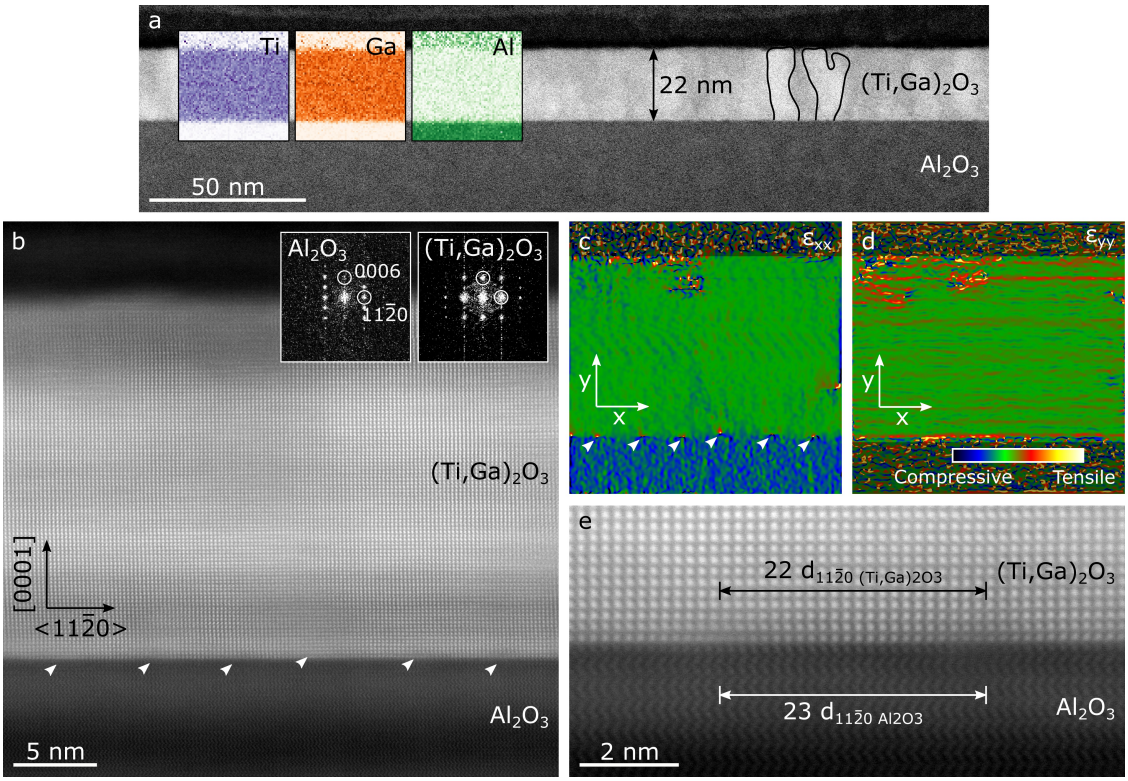

Figure 3. (**a**,**b**) HAADF-STEM images of a cross-section of sample 3%Ti, showing the $(Ti,Ga)_2O_3$ film and its interface with the sapphire substrate. EDS maps are overlaid in (**a**), showing a uniform distribution of Ti and Ga throughout the film. Two columnar regions of crystallinity in the $(Ti,Ga)_2O_3$ film are also outlined in (**a**). In inset of (**b**), the FFTs of the film and substrate confirm the corundum structure. Strain in the film, perpendicular ($\mathbf{g} = 11\bar{2}0$) (**c**) and parallel ($\mathbf{g} = 0006$) (**d**) to the growth direction, was obtained from geometrical phase analysis. Regularly spaced misfit dislocations are indicated by arrows in (**b**,**c**). (**e**) High resolution HAADF-STEM image of film-substrate interface, clearly showing 2 misfit dislocations and their separation. All images are taken along the $\langle 1\bar{1}00 \rangle$ zone axis.

Figure 5 collates the main findings of the study in terms of film composition, crystallinity and optical band gap. The decrease in band gap energy with increasing Ti concentration can be clearly seen. The figure also displays literature values of band gaps for α-Ga_2O_3, α-Ti_2O_3 and 3 common phases of TiO_2: rutile [56,57], anatase [58] and brookite [59]. The band gap measured for pure α-Ga_2O_3 is well within the range of literature values [1–5,60,61]. The linear trend in band gap with composition predicted by Vegard's law for α-$(Ti_xGa_{1-x})_2O_3$ has been plotted to guide the eye. For the samples with Ti concentration up to 5.3%, that are, the crystalline α-$(Ti_xGa_{1-x})_2O_3$ films, the optical band gap seems to follow that trend although this observation should be nuanced as it is based on just 3 data points. Over this range of compositions the band gap varies by ~270 meV. For the samples with greater Ti concentration, that are, the amorphous films, the band gap follows a different linear trend, with a shallower slope—over this range of composition the band gap varies by ~1.12 eV.

Given that the solar-blind region covers the range of band gap energies wider than 4.4 eV approximately, our results indicate that α-$(Ti_xGa_{1-x})_2O_3$ alloys could be an attractive material for solar-blind photodetector applications. Further improvement in crystal growth could lead to a broader

composition range of crystalline films, potentially allowing the production of wavelength-specific photodetectors beyond the solar-blind region.

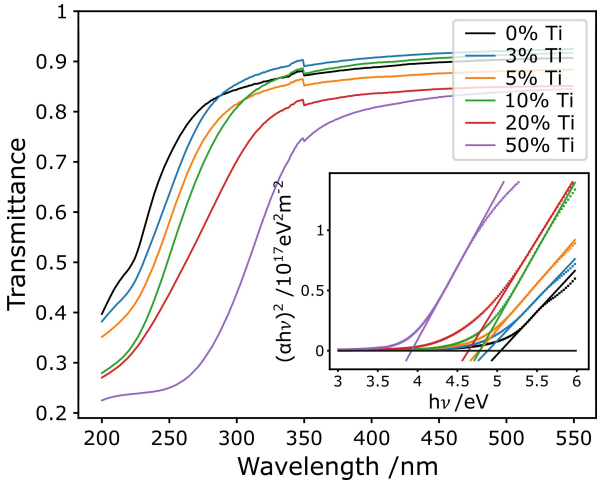

Figure 4. UV-vis transmittance spectra for the $(Ti,Ga)_2O_3$ samples. The inset shows Tauc plots evaluated using the transmittance data for each film. The straight, solid lines are the fits to the linear region of the Tauc plots and their intercepts with the dotted black line ($\alpha = 0$) gives the band gaps of the respective films.

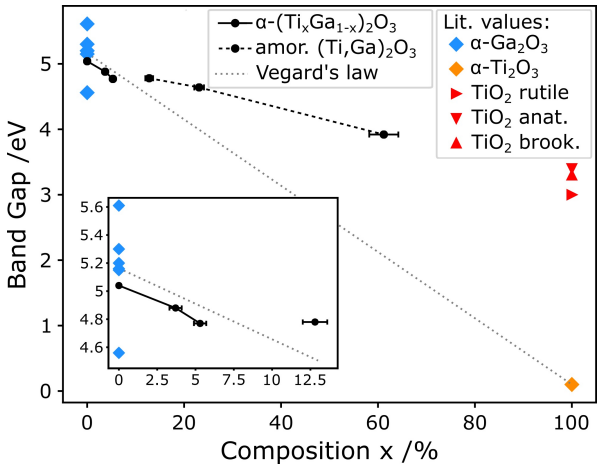

Figure 5. Plot showing the measured variation of band gap energy with the RBS composition alongside literature values of band gaps for pure oxides [1–5,30,56–62] and a Vegard's law trend between α-Ga_2O_3 and α-Ti_2O_3. The inset is an enlargement of the low Ti fraction region. The plot also differentiates between compositions based on whether crystallinity was observed by XRD.

4. Conclusions

Owing to a common crystal structure, low lattice mismatch and wide band gap difference, we investigated the use of Ti as a band gap modifier in α-Ga_2O_3. Films of $(Ti,Ga)_2O_3$ with a range of Ti concentrations were synthesized by ALD and the resulting film crystallinity and band gap characterized. The deposition of high quality α-$(Ti_xGa_{1-x})_2O_3$ films was achieved for x = 3.7%. The corundum phase was maintained in films of compositions up to x = 5.3%, although the crystalline quality degraded rapidly with increasing Ti fraction. Films with greater Ti content were amorphous. Over the range where corundum phase films were obtained, that is for $0\% \leq x \leq 5.3\%$, we report a variation of band gap energy of ~ 270 meV. Despite further effort required to increase the crystalline quality of films with greater Ti fraction, this study is a promising proof-of-principle that Ti could be used for band gap engineering of α-Ga_2O_3, and opens the path for the fabrication of wavelength-specific optoelectronic devices operating in the UV.

Author Contributions: Conceptualization, F.M. and J.R.; methodology, F.M.; validation, A.B., J.R., M.N., M.F., T.H., and A.K.; formal analysis, A.B., M.N., and F.M.; investigation, A.B., J.R., M.N., M.F., T.H., and A.K.; resources, J.R.; data curation, A.B., J.R., M.N., M.F., T.H., and A.K.; writing—original draft preparation, A.B. and F.M.; writing—review and editing, all authors; visualization, A.B., M.N. and F.M.; supervision, F.M.; project administration, P.C., T.S., R.O. and F.M.; funding acquisition, P.C., T.S. and R.O. All authors have read and agreed to the published version of the manuscript.

Funding: This project is funded by the Engineering and Physical Sciences Research Council (EPSRC Grants No. EP/P00945X/1 and No. EP/M010589/1). T.N.H. acknowledges funding from the EPSRC Centre for Doctoral Training in Graphene Technology (Grant No. EP/L016087/1). This project has received funding from the European Union's Horizon 2020 research and innovation programme under grant agreement No 823717 – ESTEEM3.

Acknowledgments: The data that support the findings of this study are openly available in PurePortal at https://doi.org/10.15129/3708a522-189e-4a41-8419-89e5f626237b.

Conflicts of Interest: The authors declare no conflict of interest. The funders had no role in the design of the study; in the collection, analyses, or interpretation of data; in the writing of the manuscript, or in the decision to publish the results.

References

1. Shinohara, D.; Fujita, S. Heteroepitaxy of corundum-structured α-Ga_2O_3 thin films on α-Al_2O_3 substrates by ultrasonic mist chemical vapor deposition. *Jpn. J. Appl. Phys.* **2008**, *47*, 7311–7313. [CrossRef]
2. Guo, D.; Zhao, X.; Zhi, Y.; Cui, W.; Huang, Y.; An, Y.; Li, P.; Wu, Z.; Tang, W. Epitaxial growth and solar-blind photoelectric properties of corundum-structured α-Ga_2O_3 thin films. *Mater. Lett.* **2016**, *164*, 364–367. [CrossRef]
3. Oshima, Y.; Villora, E.G.; Shimamura, K. Halide vapor phase epitaxy of twin-free α-Ga_2O_3 on sapphire (0001) substrates. *Appl. Phys. Express* **2015**, *8*, 055501. [CrossRef]
4. Lee, S.H.; Lee, K.M.; Kim, Y.B.; Moon, Y.J.; Kim, S.B.; Bae, D.; Kim, T.J.; Kim, Y.D.; Kim, S.K.; Lee, S.W. Sub-microsecond response time deep-ultraviolet photodetectors using α-Ga_2O_3 thin films grown via low-temperature atomic layer deposition. *J. Alloys Compd.* **2019**, *780*, 400–407. [CrossRef]
5. Roberts, J.W.; Chalker, P.R.; Ding, B.; Oliver, R.A.; Gibbon, J.T.; Jones, L.A.H.; Dhanak, V.R.; Phillips, L.J.; Major, J.D.; Massabuau, F.C.P. Low temperature growth and optical properties of α-Ga_2O_3 deposited on sapphire by plasma enhanced atomic layer deposition. *J. Cryst. Growth* **2019**, *528*, 125254. [CrossRef]
6. Zhao, X.; Wu, Z.; Guo, D.; Cui, W.; Li, P.; An, Y.; Li, L.; Tang, W. Growth and characterization of α-phase $Ga_{2-x}Sn_xO_3$ thin films for solar-blind ultraviolet applications. *Semicond. Sci. Technol.* **2016**, *31*, 065010. [CrossRef]
7. Moloney, J.; Tesh, O.; Singh, M.; Roberts, J.; Jarman, J.; Lee, L.; Huq, T.; Brister, J.; Karboyan, S.; Kuball, M.; et al. Atomic layer deposited α-Ga_2O_3 solar-blind photodetectors *J. Phys. D Appl. Phys.* **2019**, *52*, 475101. [CrossRef]
8. Gross, A.; Stangl, F.; Hoenes, K.; Sift, M.; Hessling, M. Improved Drinking Water Disinfection with UVC-LEDs for Escherichia Coli and Bacillus Subtilis Utilizing Quartz Tubes as Light Guide. *Water* **2015**, *7*, 4605–4621. [CrossRef]
9. Razeghi, M. Short-wavelength solar-blind detectors-status, prospects, and markets. *Proc. IEEE* **2002**, *90*, 1006–1014. [CrossRef]
10. Roy, R.; Hill, V.G.; Osborn, E.F. Polymorphism of Ga_2O_3 and the System Ga_2O_3—H_2O *J. Am. Chem. Soc.* **1952**, *74*, 719–722. [CrossRef]
11. Playford, H.Y.; Hannon, A.C.; Barney, E.R.; Walton, R.I. Structures of Uncharacterised Polymorphs of Gallium Oxide from Total Neutron Diffraction. *Chem. A Eur. J.* **2013**, *19*, 2803–2813. [CrossRef] [PubMed]
12. Stepanov, S.I.; Nikolaev, V.I.; Bougrov, V.E.; Romanov, A.E. Gallium Oxide: Properties and Applications—A Review. *Rev. Adv. Mater. Sci.* **2016**, *44*, 63–86.
13. Pearton, S.J.; Yang, J.; Cary, P.H.; Ren, F.; Kim, J.; Tadjer, M.J.; Mastro, M.A. A review of Ga_2O_3 materials, processing, and devices. *Appl. Phys. Rev.* **2018**, *5*, 011301. [CrossRef]
14. Kaneko, K.; Kawanowa, H.; Ito, H.; Fujita, S. Evaluation of Misfit Relaxation in α-Ga_2O_3 Epitaxial Growth on α-Al_2O_3 Substrate. *Jpn. J. Appl. Phys.* **2012**, *51*, 020201. [CrossRef]
15. Fujita, S.; Oda, M.; Kaneko, K.; Hitora, T. Evolution of corundum-structured III-oxide semiconductors: Growth, properties, and devices. *Jpn. J. Appl. Phys.* **2016**, *55*, 1202A3. [CrossRef]
16. Roberts, J.W.; Jarman, J.; Johnstone, D.; Midgley, P.; Chalker, P.; Oliver, R.; Massabuau, F.C.P. α-Ga_2O_3 grown by low temperature atomic layer deposition on sapphire. *J. Cryst. Growth* **2018**, *487*, 23–27. [CrossRef]

17. Wheeler, V.; Nepal, N.; Boris, D.; Qadri, S.; Nyakiti, L.; Lang, A.; Koehler, A.; Foster, G.; Walton, S.; Eddy, C., Jr.; et al. Phase Control of Crystalline Ga_2O_3 Films by Plasma-Enhanced Atomic Layer Deposition. *Chem. Mater.* **2020**, *32*, 1140. [CrossRef]
18. Lee, S.D.; Ito, Y.; Kaneko, K.; Fujita, S. Enhanced thermal stability of alpha gallium oxide films supported by aluminum doping. *Jpn. J. Appl. Phys.* **2015**, *54*, 030301. [CrossRef]
19. Kaneko, K.; Nomura, T.; Fujita, S. Corundum-structured α-phase Ga_2O_3-Cr_2O_3-Fe_2O_3 alloy system for novel functions. *Phys. Status Solidi C* **2010**, *7*, 2467–2470. [CrossRef]
20. Kaneko, K.; Kakeya, I.; Komori, S.; Fujita, S. Band gap and function engineering for novel functional alloy semiconductors: Bloomed as magnetic properties at room temperature with α-phase $(Ga,Fe)_2O_3$. *J. Appl. Phys.* **2013**, *113*, 233901. [CrossRef]
21. Wang, T.; Li, W.; Ni, C.; Janotti, A. Band Gap and Band Offset of Ga_2O_3 and $(Al_xGa_{1-x})_2O_3$ alloys. *Phys. Rev. Appl.* **2018**, *10*, 011003. [CrossRef]
22. Song, K.; Mohseni, M.; Taghipour, F. Application of ultraviolet light-emitting diodes (UV-LEDs) for water disinfection: A review. *Water Res.* **2016**, *94*, 341. [CrossRef] [PubMed]
23. Smith, E. The emission spectrum of hydrocarbon flames. *Proc. R. Soc. Lond. A* **1940**, *174*, 110. [CrossRef]
24. Ito, H.; Kaneko, K.; Fujita, S. Growth and Band Gap Control of Corundum-Structured α-$(Al,Ga)_2O_3$ Thin Films on Sapphire by Spray-Assisted Mist Chemical Vapor Deposition. *Jpn. J. Appl. Phys.* **2012**, *51*, 100207. [CrossRef]
25. Fujita, S.; Kaneko, K. Epitaxial growth of corundum-structured wide bandgap III-oxide semiconductor thin films. *J. Cryst. Growth* **2014**, *401*, 588–592. [CrossRef]
26. Kaneko, K.; Fujita, S.; Hitora, T. A power device material of corundum-structured α-Ga_2O_3 fabricated by MIST EPITAXY technique. *Jpn. J. Appl. Phys.* **2018**, *57*, 02CB18. [CrossRef]
27. Innocenzi, M.E.; Swimm, R.T.; Bass, M.; French, R.H.; Villaverde, A.B.; Kokta, M.R. Room-temperature optical absorption in undoped α-Al_2O_3. *J. Appl. Phys.* **1990**, *67*, 7542–7546. [CrossRef]
28. Weiher, R.L.; Ley, R.P. Optical Properties of Indium Oxide. *J. Appl. Phys.* **1966**, *37*, 299–302. [CrossRef]
29. Chi, T.C.; Sladek, R.J. Elastic Constants and the Electrical Transition in Ti_2O_3. *Phys. Rev. B* **1973**, *7*, 5080–5085. [CrossRef]
30. Li, Y.; Weng, Y.; Yin, X.; Yu, X.; Kumar, S.R.S.; Wehbe, N.; Wu, H.; Alshareef, H.N.; Pennycook, S.J.; Breese, M.B.H.; et al. Orthorhombic Ti_2O_3: A Polymorph-Dependent Narrow-Bandgap Ferromagnetic Oxide. *Adv. Funct. Mater.* **2018**, *28*, 1705657. [CrossRef]
31. Guo, Y.; Clark, S.; Robertson, J. Calculation of metallic and insulating phases of V_2O_3 by hybrid density functionals. *J. Chem. Phys.* **2014**, *140*, 054702. [CrossRef] [PubMed]
32. Al-Kuhaili, M.; Saleem, M.; Durrani, S. Optical properties of iron oxide (α-Fe_2O_3) thin films deposited by the reactive evaporation of iron. *J. Alloys Compd.* **2012**, *521*, 178–182. [CrossRef]
33. Cheng, R.; Xu, B.; Borca, C.N.; Sokolov, A.; Yang, C.S.; Yuan, L.; Liou, S.H.; Doudin, B.; Dowben, P.A. Characterization of the native Cr_2O_3 oxide surface of CrO_2. *Appl. Phys. Lett.* **2001**, *79*, 3122–3124. [CrossRef]
34. Koffyberg, F.P. Optical bandgaps and electron affinities of semiconducting Rh_2O_3(I) and Rh_2O_3(III). *J. Phys. Chem. Solids* **1992**, *53*, 1285–1288. [CrossRef]
35. Thomas, G.A.; Rapkine, D.H.; Carter, S.A.; Millis, A.J.; Rosenbaum, T.F.; Metcalf, P.; Honig, J.M. Observation of the Gap and Kinetic Energy in a Correlated Insulator. *Phys. Rev. Lett.* **1994**, *73*, 1529–1532. [CrossRef]
36. Yao, Y.; Okur, S.; Lyle, L.A.M.; Tompa, G.S.; Salagaj, T.; Sbrockey, N.; Davis, R.F.; Porter, L.M. Growth and characterization of α-, β-, and ϵ-phases of Ga_2O_3 using MOCVD and HVPE techniques. *Mater. Res. Lett.* **2018**, *6*, 268–275. [CrossRef]
37. Lee, W.E.; Lagerlof, K.P.D. Structural and electron diffraction data for sapphire (α-Al_2O_3). *J. Electron Microsc. Tech.* **1985**, *2*, 247–258. [CrossRef]
38. Zhang, K.H.L.; Lazarov, V.K.; Galindo, P.L.; Oropeza, F.E.; Payne, D.J.; Lai, H.H.C.; Egdell, R.G. Domain Matching Epitaxial Growth of In_2O_3 Thin Films on α-Al_2O_3 (0001). *Cryst. Growth Des.* **2012**, *12*, 1000–1007. [CrossRef]
39. Rice, C.E.; Robinson, W.R. Structural changes in the solid solution $(Ti_{1-x}V_x)_2O_3$ as x varies from zero to one. *J. Solid State Chem.* **1977**, *21*, 155–160. [CrossRef]
40. Di Cerbo, R.K.; Seybolt, A.U. Lattice Parameters of the α-Fe_2O_3-Cr_2O_3 Solid Solution. *J. Am. Ceram. Soc.* **1959**, *42*, 430–431. [CrossRef]

41. Coey, J.M.D. The crystal structure of Rh_2O_3. *Acta Crystallogr. Sect. B Struct. Crystallogr. Cryst. Chem.* **1970**, *26*, 1876–1877. [CrossRef]
42. McWhan, D.B.; Remeika, J.P. Metal-Insulator Transition in $(V_{1-x}Cr_x)_2O_3$). *Phys. Rev. B* **1970**, *2*, 3734–3750. [CrossRef]
43. Mott, N. Metal-insulator transition in Ti_2O_3. *J. Phys.* **1981**, *42*, 277–281. [CrossRef]
44. Manandhar, S.; Ramana, C. Direct, functional relationship between structural and optical properties in titanium-incorporated gallium oxide nanocrystalline thin films. *Appl. Phys. Lett.* **2017**, *110*, 061902. [CrossRef]
45. Manandhar, S.; Battu, A.; Tan, S.; Panat, R.; Shutthanandan, V.; Ramana, C. Effect of Ti doping on the crystallography, phase, surface/interface structure and optical band gap of Ga_2O_3 thin films. *J. Mater. Sci.* **2019**, *54*, 11526. [CrossRef]
46. Bandi, M.; Zade, V.; Roy, S.; Nair, A.; Seacat, S.; Sreenivasan, S.; Shutthanandan, S.; Van de Walle, C.; Peelaers, H.; Ramana, C. Effect of Titanium Induced Chemical Inhomogeneity on Crystal Structure, Electronic Structure, and Optical Properties of Wide Band Gap Ga_2O_3. *Cryst. Growth Des.* **2020**, *20*, 1422. [CrossRef]
47. Ritala, M.; Leskela, M.; Niinisto, L.; Haussalo, P. Titanium isopropoxide as a precursor in atomic layer epitaxy of titanium dioxide thin films. *Chem. Mater.* **1993**, *5*, 1174–1181. [CrossRef]
48. Mayer, M. *SIMNRA User's Guide for Version 7.0*; Max-Planck-Institut für Plasmaphysik: Garching, Germany, 2017.
49. Ernst Ruska-Centre for Microscopy and Spectroscopy with Electrons. *J. Large-Scale Res. Facil.* **2016**, *2*, A43. [CrossRef]
50. Hÿtch, M.J.; Snoeck, E.; Kilaas, R. Quantitative measurement of displacement and strain fields from HREM micrographs. *Ultramicroscopy* **1998**, *74*, 131–146. [CrossRef]
51. Mackus, A.J.M.; Schneider, J.R.; MacIsaac, C.; Baker, J.G.; Bent, S.F. Synthesis of Doped, Ternary, and Quaternary Materials by Atomic Layer Deposition: A Review. *Chem. Mater.* **2019**, *31*, 1142–1183. [CrossRef]
52. Coll, M.; Napari, M. Atomic layer deposition of functional multicomponent oxides. *APL Mater.* **2019**, *7*, 110901. [CrossRef]
53. Vegard, L. Die Konstitution der Mischkristalle und die Raumfüllung der Atome. Die Konstitution Der Mischkristal. *Z. Phys.* **1921**, *5*, 17. [CrossRef]
54. Denton, A.R.; Ashcroft, N.W. Vegard's law. *Phys. Rev. A* **1991**, *43*, 3161–3164. [CrossRef] [PubMed]
55. Chen, Z.; Jaramillo, T. *The Use of UV-Visible Spectroscopy to Measure the Band Gap of a Semiconductor*; Department of Chemical Engineering, Stanford University: Stanford, CA, USA, 2017.
56. Pascual, J.; Camassel, J.; Mathieu, H. Fine structure in the intrinsic absorption edge of TiO_2. *Phys. Rev. B* **1978**, *18*, 5606–5614. [CrossRef]
57. Amtout, A.; Leonelli, R. Optical properties of rutile near its fundamental band gap. *Phys. Rev. B* **1995**, *51*, 6842–6851. [CrossRef]
58. Tang, H.; Levy, F.; Berger, H.; Schmid, P.E. Urbach tail of anatase TiO_2. *Phys. Rev. B* **1995**, *52*, 7771–7774. [CrossRef]
59. Mattsson, A.; Osterlund, L. Adsorption and Photoinduced Decomposition of Acetone and Acetic Acid on Anatase, Brookite, and Rutile TiO_2 Nanoparticles. *J. Phys. Chem. C* **2010**, *114*, 14121–14132. [CrossRef]
60. Hou, Y.; Wu, L.; Wang, X.; Ding, Z.; Li, Z.; Fu, X. Photocatalytic performance of α-, β-, and γ-Ga_2O_3 for the destruction of volatile aromatic pollutants in air. *J. Catal.* **2007**, *250*, 12–18. [CrossRef]
61. Segura, A.; Artus, L.; Cusco, R.; Goldhahn, R.; Feneberg, M. Band gap of corundumlike α-Ga_2O_3 determined by absorption and ellipsometry. *Phys. Rev. Mater.* **2017**, *1*, 024604. [CrossRef]
62. Shin, S.H.; Chandrashekhar, G.V.; Loehman, R.E.; Honig, J.M. Thermoelectric Effects in Pure and V-Doped Ti_2O_3 Single Crystals *Phys. Rev. B* **1973**, *8*, 1364–1372. [CrossRef]

Publisher's Note: MDPI stays neutral with regard to jurisdictional claims in published maps and institutional affiliations.

© 2020 by the authors. Licensee MDPI, Basel, Switzerland. This article is an open access article distributed under the terms and conditions of the Creative Commons Attribution (CC BY) license (http://creativecommons.org/licenses/by/4.0/).